Anti-siting for stabilizing structure and modulating cationic/anionic redox reactions

Luyao Wang [a,b], Chu Zhang [a,b], Ting Lin [a,c], Hang Chu [a,b], Yurui Gao [d], Zhiwei Hu [e], Shu-Chih Haw [f], Chien-Te Chen [f], Chang-Yang Kuo [f,g], Xiangfei Li [a,b], Yuming Gai [h], Qinwen Guo [a,b], Ying Meng [a,c], Haoyu Zhuang [a,c], Xi Shen [a,*], Zhaoxiang Wang [a,b,c,*], Richeng Yu [a,b,c,i,*]

[a] Beijing National Laboratory for Condensed Matter Physics, Institute of Physics, Chinese Academy of Sciences, Beijing, 100190, China
[b] College of Material Science and Opto-Electronic Technology, University of Chinese Academy of Sciences, Beijing, 100190, China
[c] School of Physical Sciences, University of Chinese Academy of Sciences, Beijing, 100049, China
[d] Laboratory of Theoretical and Computational Nanoscience, National Center for Nanoscience and Technology, Chinese Academy of Sciences, Beijing, 100190, China
[e] Max Planck Institute for Chemical Physics of Solids, Dresden, 01187, Germany
[f] National Synchrotron Radiation Research Center, Hsinchu, 300092, Taiwan
[g] Department of Electrophysics, National Yang Ming Chiao Tung University, Hsinchu, 30010, Taiwan
[h] College of Electronic Engineering, South China Agricultural University, Guangzhou, 510642, China
[i] Songshan Lake Materials Laboratory, Dongguan, 523808, China

ARTICLE INFO

ABSTRACT

The layered Mn-rich oxide cathode materials with oxygen redox activity are highly appealing in sodium-ion (Na-ion) batteries because of their high energy density and low cost. However, the applications of such materials are hindered by issues such as low Mn redox potential and irreversible phase transformation. Rational modulation of the ordering of the transition metal (TM) layer can inhibit the constraints and stabilize the anionic redox reactions. Herein we introduce stable Li/Mn anti-siting in the TM layer of P2-type $Na_{0.6}Li_{0.2}Mn_{0.8}O_2$ as a strategy to create abundant Mn sites and O sites that are inequivalent to the counterpart of each in the lattice, and thus to prompt the diverse Mn and O redox. The self-locking of the anti-siting energetically inhibits the P2-O2 phase transformation and the resultant structural degradations. In addition, such modulation activates more Mn in charge compensation at high potentials. As a result, this regulation increases the reversible capacity from 104.2 mAh g^{-1} to 153.7 mAh g^{-1} and enhances the cycling stability of $Na_{0.6}Li_{0.2}Mn_{0.8}O_2$. This anti-siting strategy offers a new solution to designing cathode materials with high structural stability and high energy density.

1. Introduction

With the increasing demands for a fossil-fuel-free world, sodium-ion batteries (SIBs) are employed in applications such as grid energy storage and photovoltaic engineering [1,2]. Layered transition metal (TM) oxide cathode materials are desirable on account of their high energy density [3], among which the Mn-rich layer-structured cathode materials with lattice oxygen redox are particularly promising because of their low cost and low toxicity [4]. However, the commercialization of these materials meets inherent challenges such as low Mn redox potential and structural transformation during cycling [5]. Some of these originate from the Mn redox while some others are related to the oxygen (anionic) oxidation.

Therefore, it is vital to address these issues by stabilizing the structure and cationic/anionic redox reactions.

The adjustability of the TM layer (such as ordering/disordering, heteroatoms and their contents) makes it possible to conduct diverse regulations to modify the cationic/anionic redox [6]. On one hand, TM-modulation has been employed to address issues associated with the cation redox. For example, Li doping in the TM layer of $Na_xCu_{0.11}Ni_{0.11}Fe_{0.3}Mn_{0.48}O_2$ modulates its localized electronic structure and optimizes the TM redox [7]. Yang et al. in this group introduce TM vacancies in P2-$Na_{2/3}[Zn_{2/9}Mn_{7/9}]O_2$ to shorten the Mn-O bond, enhancing the content of the low-spin Mn^{3+} and inhibiting the P2-P'2 structural transformation [8]. On the other hand, TM regulation holds

---

* Corresponding authors.
E-mail addresses: xshen@iphy.ac.cn (X. Shen), zxwang@iphy.ac.cn (Z. Wang), rcyu@iphy.ac.cn (R. Yu).

promise in resolving issues related to the anionic (O^{2-}) redox. Substitution of Sn or Zr for Mn in $Na_{0.66}Li_{0.22}Mn_{0.78}O_2$ effectively alleviates the anisotropic Mn-O coupling and the oxygen loss [9]. Qi et al. pointed out that a honeycomb superstructure is formed in $Na_{0.6}Li_{0.2}Mn_{0.73}Fe_{0.07}O_2$ and Fe-substitution mitigates its oxygen loss and the structural transformation [10]. However, the above efforts were focused only on regulating either the Mn redox at low potentials or the oxygen redox at high potentials. Therefore, it is required to design a proper TM layer for a more desirable layered oxide.

Anti-siting (TM migration into the alkali metal (AM) layer and *vice versa*) has been employed in layered cathode materials to effectively enhance the structural stability. For example, the Ho doping in O3-type $NaMn_{1/3}Fe_{1/3}Ni_{1/3}O_2$ induces Na/Mn anti-siting and enables more O lone-pair electrons to participate in the charge compensation [11]. A Li/Ni anti-siting in $LiNi_{0.88}Co_{0.09}Al_{0.03}O_2$ suppresses the TM migration and the transformation to spinel [12]. However, some of these migrations from AM to TM layer (AM/TM anti-siting) degrade the Li/Na-ion diffusivity, structural stability and cycling performance [3,13,14]. Inspired with the gliding of the TM layer in Li_2RuO_3 driven by the minimized coulombic repulsion [15], we suppose that introducing of TM/TM anti-siting might lead to approaches for achieving more stable structures via minimizing the coulombic repulsions.

Herein, we design a Li_{TM}/Mn_{TM} anti-siting in the P2-type $Na_{0.6}Li_{0.2}Mn_{0.8}O_2$ by quenching it in liquid nitrogen. The idea was inspired with the facts that quenching at high temperature has been popularly applied to modify the atomic arrangements of materials [16,17]. The self-locked Li_{TM}/Mn_{TM} anti-siting is realized by the alternative stacking of Li and Mn in a TM layer and in the neighboring TM layer, resulting in the minimized coulombic repulsions. This modulation simultaneously enhances both the structural stabilization and the cationic and anionic redox. Meanwhile, it eliminates the negative effects of the previously reported AM/TM anti-siting strategy. The anti-sited structure elevates the Mn redox potential and increases the reversible capacity of the material. In combination with the density functional theory (DFT) calculations, we demonstrate that the anti-siting enriches the O configurations in $Na_{0.6}Li_{0.2}Mn_{0.8}O_2$ and facilitates the O oxidation, and the self-locking feature energetically restrains the phase transformation. Therefore, anti-siting is highlighted for enhancing the structural stability and redox activity of layered Mn-rich oxide cathode materials.

2. Results and discussion

2.1. Structure and Li/Mn anti-siting

P2-type $Na_{0.6}Li_{0.2}Mn_{0.8}O_2$ with ribbon-ordered superstructure was synthesized by a solid-state reaction at 900 °C for 12 h and subsequent natural cooling (sample P hereafter). Sample Q was obtained by quenching sample P in liquid nitrogen when it was naturally cooled down to 700 °C. The weak diffractions (marked with green rectangles in Fig. S1) are the fingerprints of the ribbon-ordered Li/Mn superstructure in the TM layer [18]. Fig. 1a1 shows the schematic illustrations of the structure [19], the basis for identifying the Miller indices for a crystallographic plane. The TM layer of sample P presents a ribbon-ordered arrangement in the sequence of Li-Mn-Mn-Mn-Mn.

Samples P and Q are similar in morphology (Fig. S2) and elemental composition (Table S1). However, the quenching processing results in a slightly smoother surface for sample Q. The above weak diffractions in
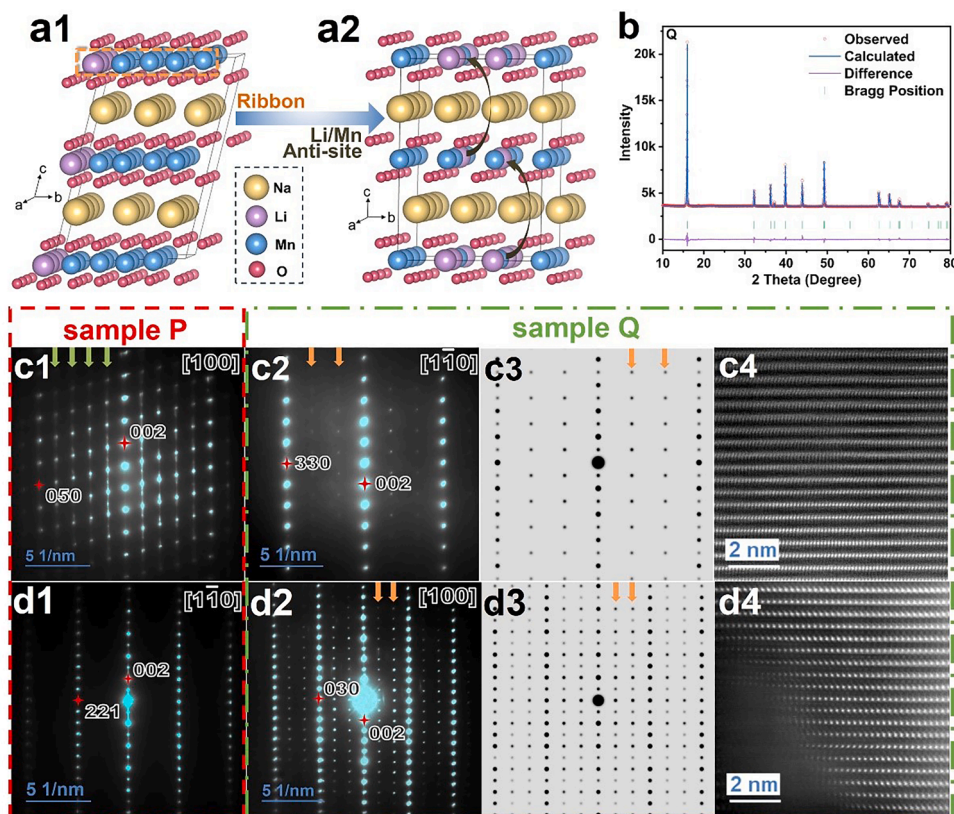

Fig. 1. The structures of samples P and Q: (a) the schematic structures of sample P (a1) and sample Q (a2) and the transformation between them; (b) the XRD pattern of sample Q and its Rietveld refinement results; the experimental SAED patterns (c1 and d1 for sample P; c2 and d2 for sample Q; the green arrows highlight the ribbon-ordered superstructure while the orange arrows highlight the new superstructure); the simulated electron diffraction patterns (c3 and d3, all based on the schematic structure with Li/Mn anti-siting) and the STEM-HAADF images (c4 and d4) for sample Q. The zone axes are the [100] and [$1\bar{1}0$] for sample Q and the equivalent zone axes for sample P.

sample P become absent in sample Q, implying that quenching destroys the TM superlattice (Fig. 1b). The Rietveld refinement to the X-ray diffraction (XRD) patterns of both samples P and Q (Table S2) indicates that they share similar lattice parameters and both can be indexed to the $P6_3/mmc$ space group [18]. Both samples are P2-type oxides with Na on the triangular prismatic sites. Therefore, anti-siting is supposed to occur during quenching. Fig. 1a2 illustrates the schematic structural diagram of sample Q. In sample Q, the alternative stacking of Li and Mn in a TM layer and in the neighboring TM layers (that is, Li-Li-Mn *vs.* Li-Mn-Li sequences and Li-Li-Mn *vs.* Mn-Mn-Li sequences) forms a self-locked Li/Mn anti-siting. Evaluation with the refined isotropic thermal displacement parameter (B_{iso}) shows that the Li/Mn mixing in sample Q is more severe than in sample P ($B_{iso}(Li) = 1.775$ for sample Q *vs.* 0.329 for sample P). This means that the ribbon-ordering in the TM layer is lost in sample Q in view of a microscale.

Some new diffractions can be observed in the selected area electron diffraction (SAED) patterns of sample Q along the [100] and [1$\bar{1}$0] zone axes (Fig. 1c and d). The green arrows highlight the diffractions of the ribbon-ordered superstructure in sample P (Fig. 1c1 and d1). Two extra rows of diffraction spots appear in sample Q along the *b*-axis in addition

to the primary diffraction spots from the $P6_3/mmc$ space group (Fig. 1c2 and d2; the orange arrows highlight the new superstructure). We constructed a Li/Mn anti-siting modulated supercell by expanding the $P6_3/mmc$ unit cell (the same as the reported P2-type Na$_{0.6}$MnO$_2$) [20] twice along the *a*-axis and three times along the *b*-axis (Fig. 1b2) on the basis of the periodicity and the extinction rule of the electron diffraction patterns; the black arrows highlight the anti-sited structure. Therefore, structural modulation is realized by anti-siting the TM ions in the TM layer (TM$_{TM}$) and the Li ions in the TM layer (Li$_{TM}$) (Li$_{TM}$/Mn$_{TM}$). The modulated supercell can be indexed to the $P1$ space group, $a = b = 8.5536$ Å, $c = 11.1421$ Å, $\alpha = \beta = 90°$, $\gamma = 120°$ (see Table S3 for more details). The simulated electron diffraction patterns along the [1$\bar{1}$0] (Fig. 1c3), [100] (Fig. 1d3), and [130] (Fig. S3b) zone axes well match the experimental SAED patterns (Fig. 1c2 and 1d2, Fig. S3a), indicating the reasonability and correctness of the above constructed supercell. To our knowledge, this is the first time when TM anti-siting is constructed in a cathode material. Comparisons of the structures (schematic) and simulated SAED patterns of the anti-siting and crystallographic disordering indicate that the anti-siting ordering structure is different from the intralayer Li/Mn disordering one (Fig. S4). It is clearly shown that
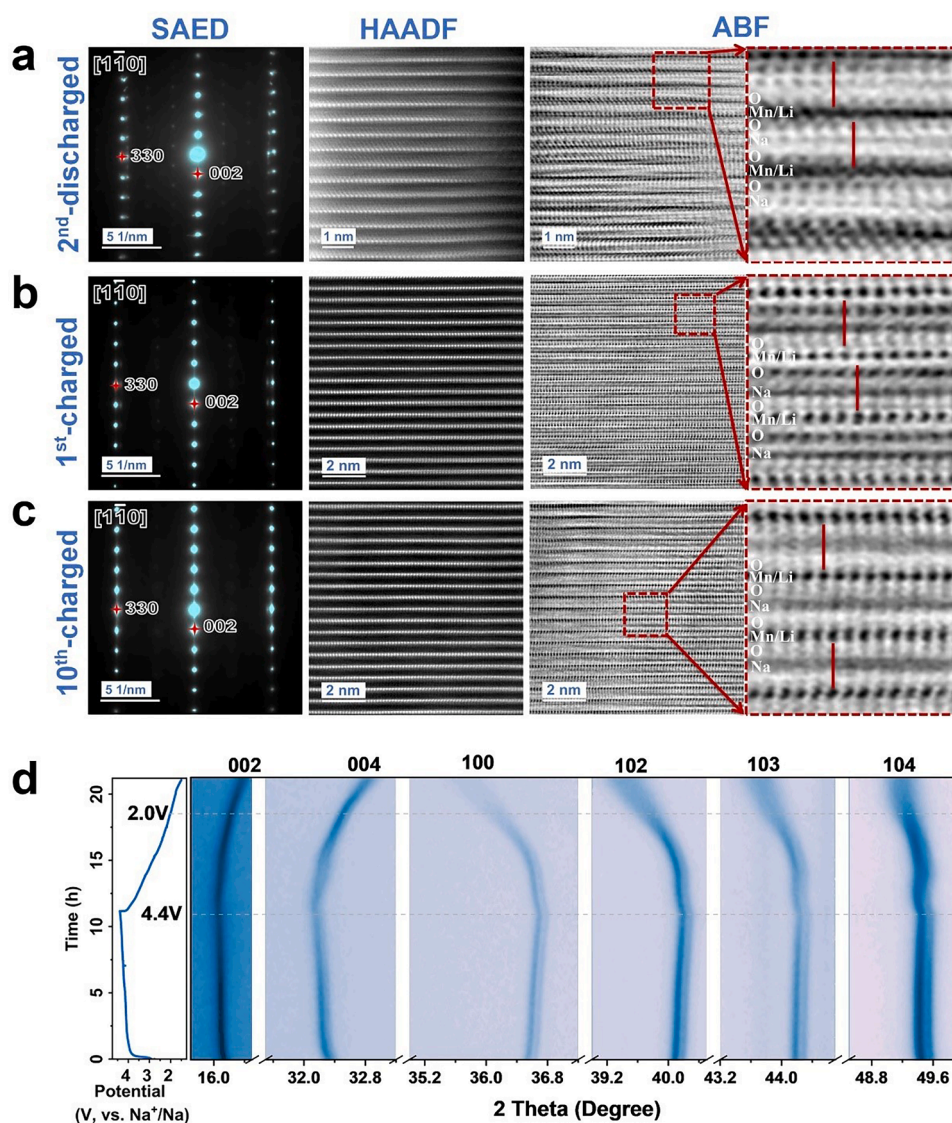

Fig. 2. The structural evolution of sample Q during cycling. The SAED, STEM-HAADF, STEM-ABF, and enlarged STEM-ABF images (from left to right) of (a) discharged to 1.5 V in the 2nd cycle, (b) the initially charged to 4.5 V, and (c) charged to 4.5 V in the 10th cycle. (d) the *in situ* XRD pattern between 1.5 and 4.4 V in the 1st cycle.
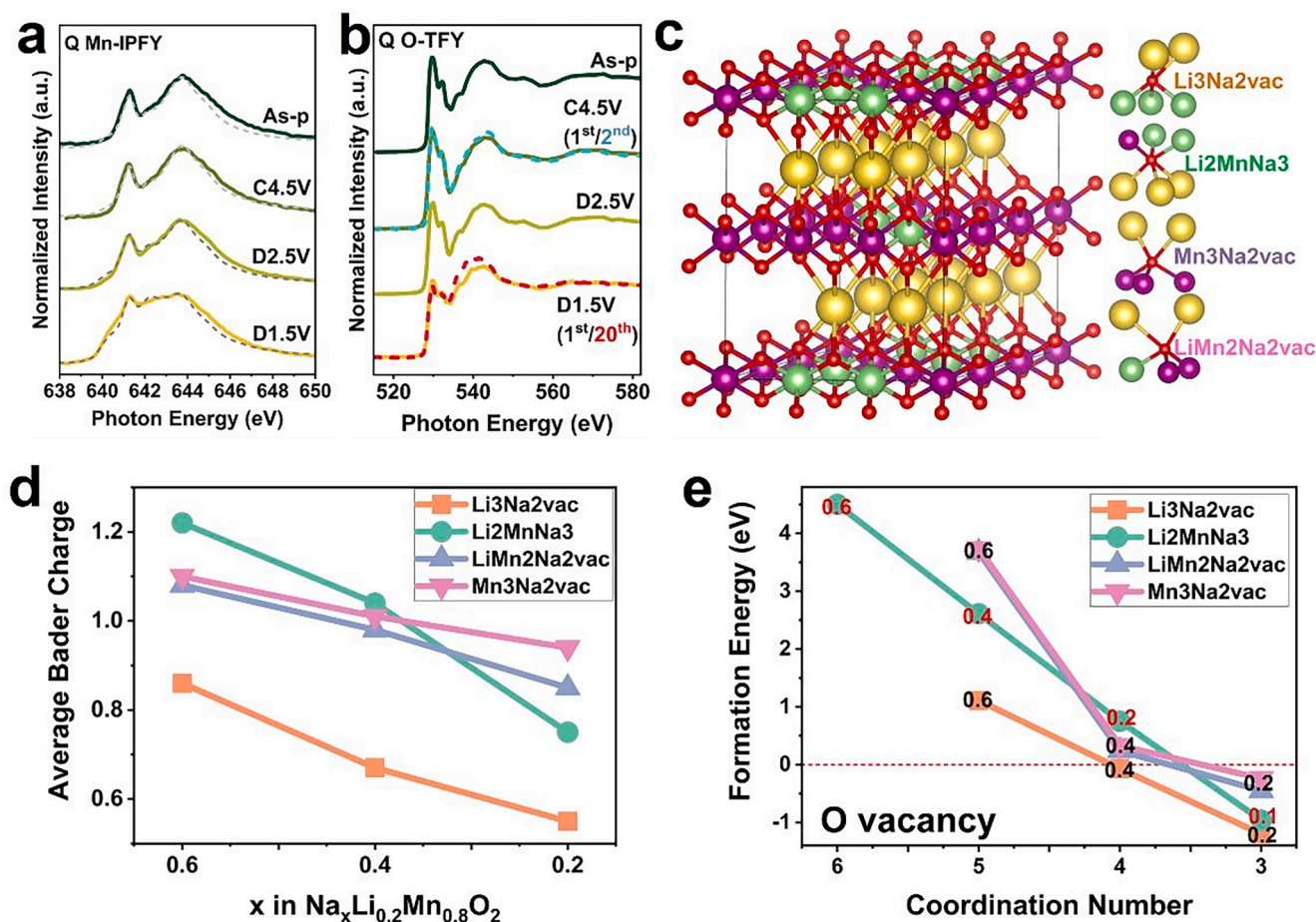
Fig. 3. The charge compensation mechanism of sample Q during cycling. (a, b) The XAS spectra of the Mn L_3-edge in the IPFY mode (a), the O K-edge in the TFY mode (b) at different states. The solid and dashed lines in (a) are the experimental and simulating results, respectively. The blue and red dashed lines in (b) are the states in the 2nd and 20th cycles, respectively. (c-e) The crystal structure of sample Q (c), the ABCs (d) and oxygen vacancy formation energies (e) of inequivalent O atoms during desodiation. The yellow ball is for Na, green for Li, purple for Mn, and red for O. The right of (c) correspondingly shows that sample Q contains four different coordination environments of O atoms, *i.e.*, O-Li3Na2vac, O-Li2MnNa3, O-Mn3Na2vac, and O-LiMn2Na2vac. While sample P only contains O-Mn3Na2vac and O-LiMn2Na2vac. The numbers in (e) indicate the Na contents in $Na_xLi_{0.2}Mn_{0.8}O_2$.

the two structures have distinct atomic coordination environments. The disordering model randomly generated by Vienna *ab initio* simulation package (VASP) [21] cannot accurately match the atomic coordination environment of the intralayer Li/Mn anti-siting. Therefore, we adopted the anti-siting structure as the fundamental model.

The scanning transmission electron microscopy-high angle angular dark field (STEM-HAADF) imaging (Fig. 1c4 and d4, Fig. S3c) verifies the well-defined P2-type layered structure of sample Q. The anti-sited structure replaces the ribbon-ordered superstructure and thus gives rise to the homogeneous contrast in the TM layer. On the other hand, sample P holds only a ribbon-ordered Li/Mn superstructure along the [100] and [001] zone axes (Fig. S5), consistent with the previous reports [18,19].

With the above discussion, we recognized anti-siting in the quenched $Na_{0.6}Li_{0.2}Mn_{0.8}O_2$ in various dimensions. XRD suggests that the anti-siting modulates the long-range (at a micron scale) ribbon-ordering within the TM layer, the STEM imaging visually displays a well-defined layered structure with the anti-sited arrangement at the atomic scale and the simulated electron diffraction pattern well agrees with the experimental SAED pattern. Therefore, we have successfully modulated the structure of the ribbon-ordered P2-$Na_{0.6}Li_{0.2}Mn_{0.8}O_2$ with Li/Mn anti-siting and confirmed this regulation. In addition, such a Li_{TM}/Mn_{TM} anti-siting structure has not been elaborated by electron microscopy before.

2.2. Self-locked TM sequence and reinforced structural stability

The structural evolutions of samples P and Q were elucidated during cycling between 1.5 and 4.5 V *vs.* Na^+/Na. XRD shows that sample Q preserves its P2-type structure characteristic of the strong (10*l*) peaks until it is charged to 4.5 V (Fig. S6). In contrast, an additional peak associated with the O2 phase appears on the right of the (002) diffraction peak of sample P in this process.

The (100) diffraction peak splits into two peaks as sample Q is discharged to 1.5 V. One of them retains its original position while the other shifts to the low angle. Despite of changes in the *a*-axis, its P2 structure is maintained in 20 cycles; no distorted phase appears (large Jahn-Teller (J-T) distortion becomes apparent in P2-type $Na_{2/3}Zn_{2/9}Mn_{7/9}O_2$, for example [8].).

In accordance with XRD, the STEM imaging shows that both samples exhibit well-defined layered structures in the bulk and on the surface at the end of the initial discharge (1.5 V) (Fig. S7). However, different from sample P in which distortions appear on the surface (Fig. S8), the P2-type structure and the anti-siting feature can still be observed in sample Q after 2 full cycles (Fig. 2a). The disparity between these two samples becomes more obvious after 10 cycles (Fig. S9 and S10). Spinel domains are observed on the surface of sample P (Fig. S9h). In contrast, the STEM imaging confirms the preservation of the P2 structure of the discharged sample Q (10 cycles; Fig. S11c).

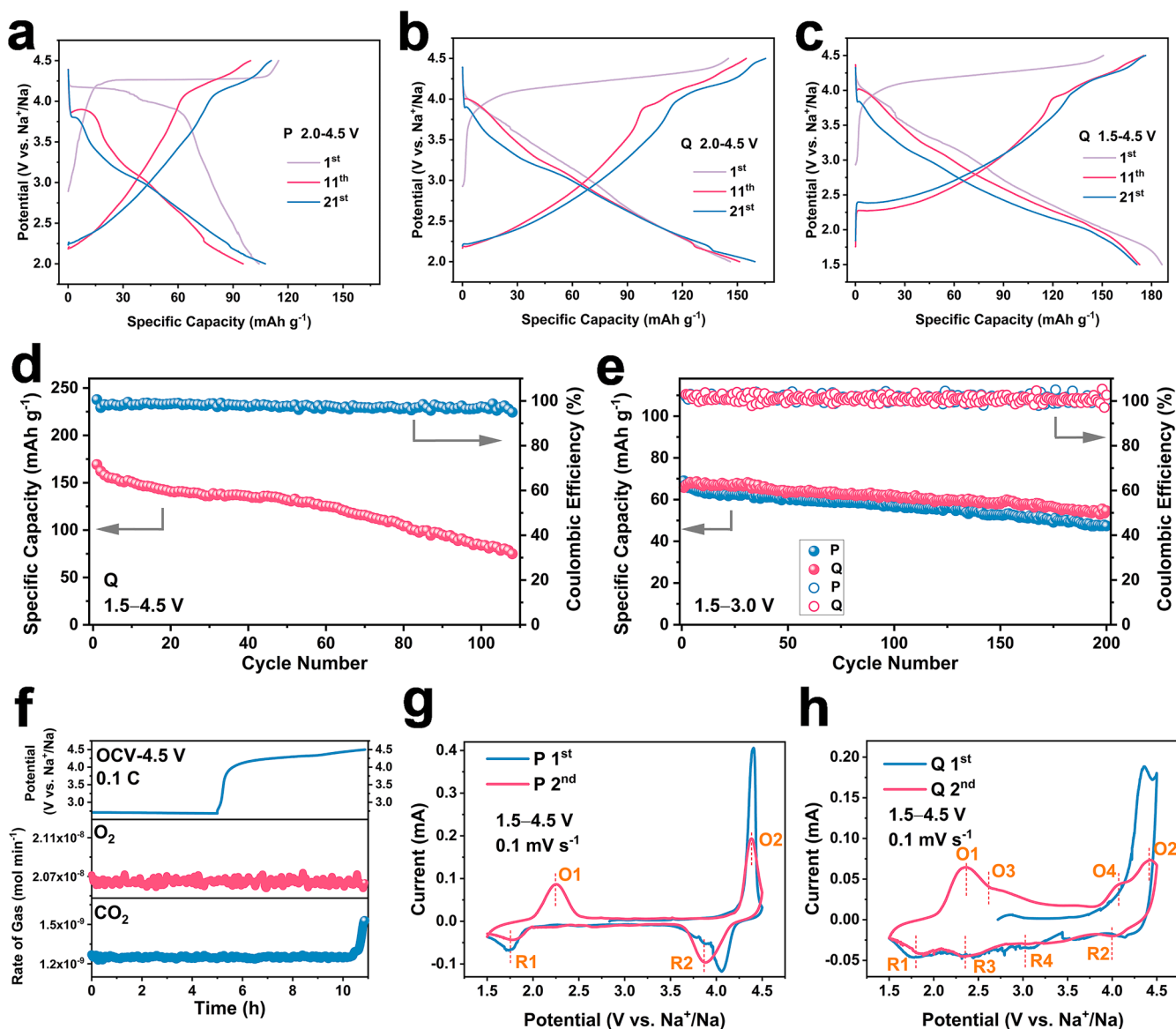The charged samples were tested to illuminate the impact of anti-

Fig. 4. Comparison of the electrochemical performances. (a, b) The charge/discharge profiles of sample P (a) and sample Q (b) in the 1st, 11th, and 21st cycles between 2.0 and 4.5 V at a current density of 20 mA g^{-1}. (c) The charge/discharge profiles of sample Q in the 1st, 11th, and 21st cycles between 1.5 and 4.5 V at a current density of 20 mA g^{-1}. (d) The cycling performance of sample Q between 1.5 and 4.5 V at a current density of 100 mA g^{-1}. (f) The *operando* DEMS of sample Q between OCV and 4.5 V in the 1st cycle at a current density of 20 mA g^{-1}. (e) The cycling performances between 1.5 and 3.0 V at a current density of 20 mA g^{-1}. (g, h) The CV curves of sample P (g) and sample Q (h) between 1.5 and 4.5 V in the 1st and 2nd cycles at a scan rate of 0.1 mV s^{-1}.

siting on the P2-O2 phase transformation at high potentials. Spinel-like domains were observed on the surface of sample P (10 cycles; Fig. S9a). Many cracks and voids appear in the bulk (Fig. S9b to f) due to the large internal strain accumulated with the irreversible P2-O2 phase transformation as a result of gliding of the TM slabs [22,23]. Meanwhile, the ribbon-ordering and TM-disordering regions coexist in the bulk (Fig. S10). These demonstrate the poor structural stability and the structural degradation of sample P during cycling. On the contrary, the enlarged STEM-angular bright field (STEM-ABF) imaging demonstrates the effective mitigation of the P2-O2 phase transformation (Fig. 2b, c), in agreement with XRD. Only negligible shrinkage is observed in the TM layer spacing on the surface (Fig. S11a, b).

Extended X-ray absorption fine structure (EXAFS) was conducted to characterize the coordination environment of Mn (Fig. S12). The amplitude of the peak is related to the coordination number around the central atom (Mn) while the peak position is related to the radius of the coordination sphere [24,25]. Therefore, the peaks at ~1.5 Å and ~2.5 Å

are assigned to the TM-O bonding (in the first coordination sphere) and the TM-TM bonding (in the second coordination sphere), respectively. As the cells are charged to 4.5 V, the intensity for the Mn-O bonding peak in sample P apparently declines due to the O oxidation and structural disordering [26,27]. In contrast, the better preservation of the Mn-O bond intensity in sample Q is attributed to the mitigated loss of oxygen upon charging [26], as is supported with the gas evolution test by the differential electrochemical mass spectroscopy (DEMS; Fig. 4f). Meanwhile, the variation of the Mn-O peak position is negligible in sample Q because of the mitigated structural disordering [27]. The Mn-TM peaks of samples P and Q shift towards the low angles due to the decreased ionic radius after oxidation. As these two samples are discharged to 1.5 V, the intensities of the peaks become weak because of the structural disordering, which can be related to the formation of Mn^{3+} [28]. The peak positions shift towards the large distance (bond length), deriving from the elongation of the Mn-O and Mn-TM bonds after Mn reduction. The peak position varies more for sample Q because of the

deeper reduction of its Mn ions than that of sample P.

In situ XRD was carried out to compare the structural evolution in the initial cycle between 1.5 and 4.4 V (Fig. 2d). The (002) and (004) diffraction peaks shift to the low angles due to the increased repulsion between the adjacent oxygen layers after Na$^+$ extraction. Trace for the P2-O2 transformation is not observed in sample Q. The absence of the phase transformation maintains in the subsequent discharge and cycling. The (002) diffraction peak shifts to the high angle due to the decreased O—O repulsion after the re-insertion of the Na$^+$ ions. The Mn reduction results in the elongation of the Mn-O bond (the (100) diffraction peak shifts to low angle). These *in situ* observations are consistent with the *ex situ* XRD results.

On the basis of the $3 \times 4 \times 2$ supercells of Na$_{0.6-x}$Li$_{0.2}$Mn$_{0.8}$O$_2$ ($x =$ 0.4; corresponding to *ca.* 4.5 V *vs.* Na$^+$/Na for samples in Fig. 1a, *ab initio* density functional theory (DFT) calculations were carried out to understand the anti-siting enhanced structural stability. The *ab* initio molecular dynamics (AIMD) simulations reveal that Mn migration to the Na layer only occurs in the ribbon-ordered structure when the structure becomes stable after 1 ps (Fig. S13). Meanwhile, the climbing image-nudged elastic band (CI-NEB) calculations indicate that the energy barrier for Mn migration to the Na layer in the anti-sited Na$_{0.2}$Li$_{0.2}$Mn$_{0.8}$O$_2$ (4.4 eV) is higher than in the ribbon-ordered Na$_{0.2}$Li$_{0.2}$Mn$_{0.8}$O$_2$ (2.8 eV) (Fig. S14). In addition, the anti-sited arrangement hinders the P2-O2 phase transformation (Fig. S15). These interpret the anti-siting enhanced structural stability. That is, the anti-siting restricts the Mn migration and the P2-O2 phase transformation at the deeply desodiated state. Therefore, the anti-sited sample Q exhibits a stable structure and keeps a single-phase reaction during cycling.

2.3. Enhanced charge compensation

Soft X-ray absorption spectroscopy (XAS; Fig. 3a-b and S16a-b) at the Mn *l*-edge and the O *K*-edge were performed to investigate the charge compensation mechanism during cycling. The energy position and multiplet spectral feature of the 3d TM $L_{2,3}$-edge sXAS spectra are highly sensitive to their valence state [29,30] and local environment [31-33]. Here, we use an inverse partial fluorescence yield (IPFY) mode, which is bulk-sensitive, but self-absorption free as compared to total fluorescence yield (TFY). In case of mixed valence Mn oxide, the average valence state can be obtained by simple supposition of spectra from different valence states [34,35]. We have found slightly more Mn^{3+} ions in the bulk of the as-prepared sample Q than in sample P (4.1% *vs.* 3.4%; see the simulating results in Fig. S17 with LaMnO$_3$ and Li$_2$MnO$_3$ as the Mn^{3+} and Mn^{4+} references). The Mn^{3+} ions are oxidized to Mn^{4+} as the cell is charged to 4.5 V, contributing extra capacity in the initial charge (Fig. 4a). After discharge, more Mn^{3+} ions can be detected in the 1.5 V discharged sample Q than in sample P, due to the activation of more Mn^{4+} ions for reduction in the bulk of sample Q (40.9% *vs.* 13.1%; Fig. S17). The activation of Mn redox is supported with the following electrochemical test (Fig. 4c). Therefore, more Mn^{3+} ions are generated in the bulk of the anti-sited sample Q for charge compensation.

The O *K*-edge spectra were obtained using the bulk-sensitive TFY mode (Fig. 3b). The pre-edge peaks originate from the transition from O 1s core level to the unoccupied O 2p states hybridized with Mn 3d orbitals [36]. The energy position of the pre-edge peaks shifts to the low energy and the spectral intensity of the pre-edge peaks increases with the increase in the valence state of the 3d element [36,37], therefore the increase or decrease in the spectral weight of the pre-edge peak can generally be used to judge the variation in the valence state of 3d element [38-40]. The peaks at lower energy (~529.6 eV) and higher energy (~531.9 eV) stand for the t$_{2g}$↓e$_g$↑ and e$_g$↓ related orbitals, respectively [34,41]. One can see that the intensity of the pre-edge peaks increases as the cells are charged to 4.5 V. Comparison of the pre-edge intensity of the as-prepared and the initially charge samples (both P and Q) indicates that the charging-induced increase of the electron holes

in the oxygen atoms is more significant in sample Q than in sample P (Fig. S16c). When sample Q is recharged to 4.5 V, the O *K*-edge is similar to the counterpart in the initial charge, indicating the reversible oxygen redox (blue dashed line in Fig. 3b). During discharging, the intensity of the pre-edge peaks decreases on account of the reoccupied O 2p states and the reduced valence of Mn [42]. After 20 full cycles, the decreased intensity of the pre-edge peaks indicates that the Mn valence in the 20th discharged sample Q is slightly lower than that in the 1st discharged sample (red dashed line in Fig. 3b). In addition, the weak peak at *ca.* 533.5 eV is related to the carbonaceous component (Na$_2$CO$_3$ or cathode-electrolyte interphase (CEI) layer) on the surface of as-prepared sample Q; it disappears after charging [7].

The Mn *K*-edge of XANES can be used to study the valence state of Mn (Fig. S18) [43,44]. The absorption edges (at ~0.7 of normalized intensity) [45,46] of as-prepared sample P and Q are similar, demonstrating their similar valence states of Mn. After charging, the shape of the main peak, which mainly represents information of crystal structure, shows the more significant change in sample P than that in sample Q, indicating the larger distortion of its local structure during Na$^+$ extraction in the former [24]. When the cells are discharged to 1.5 V, the shifting of the absorption edge to the low energy indicates a decrease in the low valence state of Mn ions in line with the above simulating XAS results (Fig. S17) [47].

In order to reveal the mechanism of the improved oxygen charge compensation in sample Q, density functional theory (DFT) calculations were conducted. Fig. S19 compares the density of states (DOS) of samples P (Fig. S19a, c and e) and Q (Fig. S19b, d and f). The Mn 3d band near the Fermi level is split in the anti-sited structure. This facilitates the charge transfer from the O 2p band to the Mn 3d band above the Fermi level [11]. In addition, the decrease of the band gap in the projected density of states (pDOS) facilitates the electronic conductivity of the anti-sited sample Q.

On the basis of the structural models of samples P and Q (Fig. 1a and 3c), the anti-sited sample Q contains O-Li3Na2vac, O-Li2MnNa3, O-LiMn2Na2vac and O-Mn3Na2vac configurations, while the ribbon-ordering sample P only contains O-LiMn2Na2vac and O-Mn3Na2vac configurations ("vac" for vacancy on Na site and "Na, Li, Mn, and 2, 3" are the atoms that are coordinated with O and the corresponding co-ordination numbers, "Na and vac" are omitted after here). Fig. 3d shows that the decrease of the average Bader charge of oxygen (O-ABC) is more significant in the O-Li3 and O-Li2Mn configurations upon sodium extraction. As a result, the oxygen in sample Q is prone to be oxidized. Therefore, it is clear that the oxygen configuration in the anti-sited structure enhances the oxygen oxidation, in accordance with the above DOS calculations. In addition, the formation energy of the oxygen vacancies in the O-Li2Mn remains positive when 0.4 Na$^+$ ions are extracted from Na$_{0.6}$Li$_{0.2}$Mn$_{0.8}$O$_2$ (Fig. 3e). Thus, the oxygen in the O-Li2Mn configuration is both highly oxidation-active and stable upon oxygen oxidation. However, the oxygen vacancy formation energy becomes negative for the O-Li3, O-LiMn2, and O-Mn3 configurations when 0.4 Na$^+$ ions are extracted from Na$_{0.6}$Li$_{0.2}$Mn$_{0.8}$O$_2$, which may lead to the oxygen loss [13]. Fortunately, only 1/18 of the total oxygen is in the O-Li3 configuration with the lowest formation energy in sample Q (Fig. S20). One sixth of the oxygen atoms are in the O-Li2Mn configuration, making it more difficult to form oxygen vacancy. However, further extraction of Na$^+$ ions (0.5) from Na$_{0.6}$Li$_{0.2}$Mn$_{0.8}$O$_2$ results in the negative oxygen vacancy formation energy in the O-Li2Mn configuration.

2.4. Elevated electrochemical performances

The voltage curves of sample P and sample Q in the 1st, 11th and 21st cycles between 2.0 and 4.5 V at a current density of 20 mA g^{-1} were compared in Fig. 4a, b. Sample Q exhibits a higher charge capacity than sample P (145.1 *vs.* 114.8 mAh g^{-1}), consistent with the improved charge compensations of the lattice oxygen and the presence of more

low-valence Mn ions in sample Q. No discernible O_2 is detected by the *operando* DEMS up to 4.5 V (Fig. 4f), indicating the stability of lattice oxygen during the oxygen oxidation. The CO_2 signal near the end of the initial charging process is attributed to the electrolyte decomposition at high potentials and/or its reaction with the activated oxygen. The CO_2 gassing rate in sample Q is $\sim 0.3 \times 10^{-9}$ mol min^{-1}, lower than the reported value in $Na_{2/3}[Zn_{2/9}Mn_{7/9}]O_2$ and $Na_{2/3}[Mg_{0.28}Mn_{0.72}]O_2$ [8, 48]. On the contrary, O_2 and CO_2 were detected at *ca.* 4.3 V in the ribbon-ordered $Na_{0.6}Li_{0.2}Mn_{0.8}O_2$ during charging [10]. These agree well with the suppressed decline of the Mn-O coordination numbers (Fig. S12). When the cell is discharged to 2.0 V, sample Q gives a discharge capacity of 146.1 mAh g^{-1} because its Mn and O ions participate in charge compensation. In contrast, sample P exhibits a capacity of 104.2 mAh g^{-1}. The difference is attributed to the involvement of more Mn ions in charge compensation (reduction) in sample Q, which agrees with the sXAS results (Fig. S17). The good performance of sample Q maintains in the 21st cycle (159.6 *vs.* 107.6 mAh g^{-1}). The discharge capacity increases due to the gradual activation of Mn^{4+} to Mn^{3+} during cycling, which is related to some changes in *ab* plane at high potentials as previously reported in $Na_{0.6}Li_{0.2}Mn_{0.8}O_2$ [49].

Sample Q shows a much higher initial discharge capacity (186.3 mAh g^{-1}) than sample P (151.2 mAh g^{-1}) as the discharge cutoff potential is extended to 1.5 V (Fig. 4c and S21). Sample Q maintains its dominance in capacity within this wide potential window (1.5~4.5 V), with a capacity of 171.1 mAh g^{-1} compared to 142.4 mAh g^{-1} in the 21st cycle. These are attributed to the excellent structural stability of sample Q. The capacity retention of sample Q is 53.0% after 100 cycles at a current density of 100 mA g^{-1} (Fig. 4d).

Only Mn redox is expected to contribute to the charge compensation between 1.5 and 3.0 V (Fig. 4e). Hence, a large number of Mn^{3+} ions are generated and could bring structural distortions (such as the J-T effect) and thus induce the capacity decay [8]. The stabilized structure of sample Q guarantees an improved capacity retention after 200 cycles than sample P (80.74% *vs.* 72.14%). The inequivalent Mn sites of the anti-sited sample Q (supported by the calculated magnetic moment in Fig. S23) could contribute to the improved stability in the low potential window.

The cyclic voltammetry (CV) of samples P and Q were recorded between 1.5 and 4.5 V to evaluate the redox mechanism (Fig. 4g, h). The Mn redox (the O1 and R1 peaks) and the ribbon-ordering induced lattice oxygen redox (the O2 and R2 peaks; at 4.38 V and 4.06 V) couples can be observed in sample P. The intensity of R2 peak significantly becomes weak in the 2nd cycle due to the stacking transformation from -α-β- to -α-γ- that hinders the accommodation of Na$^+$ below 4.5 V [19].

The voltage gaps of O1-R1 and O2-R2 couples in sample Q are similar to those of their counterparts in sample P, but the intensities in sample Q are weaker. The decline in intensity is attributed to the appearance of other new Mn and O redox peaks as follows. Firstly, the small oxidation peak (at 2.85 V) in the first charge represents the oxidation of the low-valence Mn in the as-prepared sample Q (Fig. 3a). Secondly, with the diversification of the O configurations (O-LiMn2 and extra O-Li2Mn) in sample Q, the oxygen oxidation occurs in a broader potential range (the O2 and O4 peaks), in accordance with the above calculated O ABCs. The oxygen in the O-Li2Mn configuration (coordinated with 2 Li$^+$ ions) tends to lose more electrons than in the O-LiMn2 configuration (coordinated with 1 Li$^+$ ion), thereby lowering the oxygen oxidation potential [50]. That is, the O4 peak appears at a lower potential (at 3.88 V) in sample Q than the O2 peak in sample P (4.06 V) and the O2 peak in sample Q. Therefore, the O-Li2Mn configuration facilitates the oxygen oxidation in the anti-sited sample Q.

The O1/R1 peaks and the O3/R3 peaks are related to the Mn redox arising from the multiple Mn sites, as observed in other reported materials [51]. Fig. S22 indicates that sample Q contains one extra Mn site (the adjacent atoms are Li3Mn3) compared to sample P. The abundant inequivalent Mn sites are supported with the DFT-calculated magnetic moments of Mn ions in ribbon-ordered and anti-sited samples at the

sodiated states (Fig. S23). The anti-sited structure exhibits discrete magnetic moments, indicating the different electronic structures or valence states of Mn. Generation of low-spin Mn^{3+} with fewer unpaired electrons could contribute to the lower magnetic moment in the anti-sited sample. In contrast, the ribbon-ordered structure has uniform Mn sites, resulting in its uniform magnetic moments and single Mn redox couple. Therefore, there are more inequivalent Mn sites in the anti-sited sample and thus the Mn redox is supposed to be more diversified. In addition, the anti-sited structure elevates the Mn redox potentials (O3 at 2.61 V and R3 at 2.34 V), thus addressing the issue of low-potential Mn redox (at $\sim$2.0 V) [52].

It should be noted that, despite of the complicated redox reactions, the redox peaks of sample Q still persist in the CV profiles after 12 cycles (Fig. S24). The R3 peak for the Mn reduction at high potential keeps stable in position and in intensity. Surprisingly, the O4 and R4 peaks also maintain notable intensities. Such smooth and diversified redox behavior arises from the stabilized anti-sited structure that alleviates the phase transformation and other distortions. Therefore, the diversified and stabilized redox reactions of Mn and O are verified, which can be related to the above enhanced structures and improved charge compensations.

3. Conclusion

We propose Li/Mn anti-siting in the TM layer of P2-type $Na_{0.6}Li_{0.2}Mn_{0.8}O_2$ cathode material and verify such a structure in multiple dimensions and scales. The self-locking of the anti-siting energetically inhibits the P2-O2 phase transformation and elongates the cycle life of the material. The introduction of anti-siting constructs inequivalent Mn sites and extra oxygen configurations, leading to the diverse and reversible oxygen redox. This strategy breaks down the baffles such as low redox potential of Mn and irreversible phase transformation. On one hand, more Mn ions are activated to participate in the charge compensation and the potential of the reversible Mn redox is elevated in the anti-sited material, beneficial for boosting the specific capacity and the energy density of the cathode material. On the other hand, the designed O-Li2Mn in the anti-sited structure lowers the oxygen oxidation potential, alleviating the electrolyte decomposition at high potentials. Consequently, the anti-sited modulation stabilizes the structure and enhances both the cationic and anionic redox. We provide a feasible strategy to simultaneously activate the reversible cationic/anionic redox and enhance the structural stability, and shed insights for overcoming some of the intrinsic obstacles towards high-energy-density batteries.

CRediT authorship contribution statement

Luyao Wang: Writing – original draft, Investigation, Formal analysis, Conceptualization. **Chu Zhang:** Software. **Ting Lin:** Methodology. **Hang Chu:** Formal analysis. **Yurui Gao:** Software. **Zhiwei Hu:** Investigation, Formal analysis. **Shu-Chih Haw:** Investigation, Formal analysis. **Chien-Te Chen:** Formal analysis, Investigation. **Chang-Yang Kuo:** Formal analysis, Investigation. **Xiangfei Li:** Investigation. **Yuming Gai:** Investigation. **Qinwen Guo:** Investigation. **Ying Meng:** Investigation. **Haoyu Zhuang:** Investigation. **Xi Shen:** Writing – review & editing, Supervision, Conceptualization. **Zhaoxiang Wang:** Writing – review & editing, Supervision, Conceptualization. **Richeng Yu:** Writing – review & editing, Supervision, Conceptualization.

Declaration of competing interest

The authors declare that they have no known competing financial interests or personal relationships that could have appeared to influence the work reported in this paper.

Data availability

Data will be made available on request.

Acknowledgements

Supplementary materials

Supplementary material associated with this article can be found, in the online version, at doi:10.1016/j.ensm.2024.103479.

References

[1] E. Goikolea, V. Palomares, S. Wang, I.R. de Larramendi, X. Guo, G. Wang, T. Rojo, Na-ion batteries—approaching old and new challenges, Adv. Energy Mater. 10 (2020) 2002055, https://doi.org/10.1002/aenm.202002055.

[2] H. Yao, H. Li, B. Ke, S. Chu, S. Guo, H. Zhou, Recent progress on honeycomb layered oxides as a durable cathode material for sodium-ion batteries, Small Methods 7 (2023). https://www.ncbi.nlm.nih.gov/pubmed/36843219.

[3] W. Zuo, A. Innocenti, M. Zarrabeitia, D. Bresser, Y. Yang, S. Passerini, Layered oxide cathodes for sodium-Ion batteries: storage mechanism, electrochemistry, and techno-economics, Acc. Chem. Res. 56 (2023) 284. https://www.ncbi.nlm.nih.gov/pubmed/36696961.

[4] H. Ren, H. Li, Q. Ni, Y. Bai, H. Zhao, C. Wu, Unraveling anionic redox for sodium layered oxide cathodes: breakthroughs and perspectives, Adv. Mater. 34 (2021) e2106171. https://www.ncbi.nlm.nih.gov/pubmed/34783392.

[5] K. Wang, H. Zhuo, J. Wang, F. Poon, X. Sun, B. Xiao, Recent advances in Mn-rich layered materials for sodium-ion batteries, Adv. Funct. Mater. 33 (2023), https://doi.org/10.1002/adfm.202212607.

[6] U. Maitra, A.K. Das, Oxygen redox intercalation cathodes: the fundamentals and strategies to resolve the challenges, ACS Appl. Energy Mater. 5 (2022) 4522, https://doi.org/10.1021/acsaem.1c04112.

[7] F. Ding, H. Wang, Q. Zhang, L. Zheng, H. Guo, P. Yu, N. Zhang, Q. Guo, F. Xie, R. Dang, Y. Lu, R. Xiao, L. Chen, Y.S. Hu, Tailoring electronic structure to achieve maximum utilization of transition metal redox for high-entropy Na layered oxide cathodes, J. Am. Chem. Soc. 145 (2023) 13592. https://www.ncbi.nlm.nih.gov/pubmed/37312411.

[8] L. Yang, Z. Liu, X. Shen, S. Li, Z. Hu, Q. Kong, J. Ma, J. Li, H.-J. Lin, C.-T. Chen, J.-M. Chen, S.-C. Haw, X. Wang, R. Yu, Z. Wang, L. Chen, Effect of vacancy-tailored Mn^{3+} spinning on enhancing structural stability, Energy Storage Mater. 44 (2022) 231, https://doi.org/10.1016/j.ensm.2021.10.024.

[9] C. Zhao, C. Li, Q. Yang, Q. Qiu, W. Tong, S. Zheng, J. Ma, M. Shen, B. Hu, Anionic redox reaction in Na-deficient layered oxide cathodes: role of Sn/Zr substituents and in-depth local structural transformation revealed by solid-state NMR, Energy Storage Mater. 39 (2021) 60. https://www.sciencedirect.com/science/article/pii/S2405829721001495.

[10] X. Qi, L. Wu, Z. Li, Y. Xiang, Y. Liu, K. Huang, E. Yuval, D. Aurbach, X. Zhang, Superstructure variation and improved cycling of anion redox active sodium manganese oxides due to doping by iron, Adv. Energy Mater. 12 (2022), https://doi.org/10.1002/aenm.202202355.

[11] Y. Yu, J. Zhang, R. Gao, D. Wong, K. An, L. Zheng, N. Zhang, C. Schulz, X. Liu, Triggering reversible anion redox chemistry in O3-type cathodes by tuning Na/Mn anti-site defects, Energy Environ. Sci. 16 (2023) 584, https://doi.org/10.1039/D2EE03874A.

[12] W. Yang, H. Li, D. Wang, C. Xu, W. Xiang, Y. Song, F. He, J. Zhang, B. Zheng, B. Zhong, Z. Wu, X. Guo, Ta induced fine tuning of microstructure and interface enabling Ni-rich cathode with unexpected cyclability in pouch-type full cell, Nano Energy 104 (2022), https://doi.org/10.1016/j.nanoen.2022.107880.

[13] F. Zhang, N. Qin, Y. Li, H. Guo, Q. Gan, C. Zeng, Z. Li, Z. Wang, R. Wang, G. Liu, S. Gu, H. Huang, Z. Yang, Y. Deng, Z. Lu, Phytate lithium as a multifunctional additive stabilizes $LiCoO_2$ to 4.6 V, Energy Environ. Sci. 16 (2023) 4345, https://doi.org/10.1039/D3EE01209C.

[14] M. Reynaud, J. Serrano-Sevillano, M. Casas-Cabanas, Imperfect battery materials: a closer look at the role of defects in electrochemical performance, Chem. Mater. 35 (2023) 3345, https://doi.org/10.1021/acs.chemmater.2c03481.

[15] M. Han, Z. Liu, X. Shen, L. Yang, X. Shen, Q. Zhang, X. Liu, J. Wang, H.-J. Lin, C.-T. Chen, C.-W. Pao, J.-L. Chen, Q. Kong, X. Yu, R. Yu, L. Gu, Z. Hu, X. Wang, Z. Wang, L. Chen, Stacking faults hinder lithium insertion in Li_2RuO_3, Adv. Energy Mater. 10 (2020) 2002631, https://doi.org/10.1002/aenm.202002631.

[16] J. Lee, Y. Gong, L. Gu, B. Kang, Long-term cycle stability enabled by the incorporation of Ni into Li_2MnO_3 phase in the Mn-based Li-rich layered materials, ACS Energy Lett. 6 (2021) 789, https://doi.org/10.1021/acsenergylett.1c00057.

[17] L. Junghwa, Z. Qinghua, K. Jieun, D. Nicolas, A. Maxim, J. Mihee, Y. Won-Sub, G. Lin, K. Byoungwoo, Controlled atomic solubility in Mn-rich composite material to achieve superior electrochemical performance for Li-ion batteries, Adv. Energy Mater. 10 (2019), https://doi.org/10.1002/aenm.201902231.

[18] R.A. House, U. Maitra, M.A. Pérez-Osorio, J.G. Lozano, L. Jin, J.W. Somerville, L. C. Duda, A. Nag, A. Walters, K.-J. Zhou, M.R. Roberts, P.G. Bruce, Superstructure control of first-cycle voltage hysteresis in oxygen-redox cathodes, Nature 577 (2020) 502, https://doi.org/10.1038/s41586-019-1854-3.

[19] A. Gao, Q. Zhang, X. Li, T. Shang, Z. Tang, X. Lu, Y. Luo, J. Ding, W.H. Kan, H. Chen, W. Yin, X. Wang, D. Xiao, D. Su, H. Li, X. Rong, X. Yu, Q. Yu, F. Meng, C. Nan, C. Delmas, L. Chen, Y.-S. Hu, L. Gu, Topologically protected oxygen redox in a layered manganese oxide cathode for sustainable batteries, Nat. Sustain. 5 (2022) 214, https://doi.org/10.1038/s41893-021-00809-0.

[20] A. Caballero, L. Hernán, J. Morales, L. Sánchez, J.Santos Peña, M.A.G. Aranda, Synthesis and characterization of high-temperature hexagonal P2-$Na_{0.6}MnO_2$ and its electrochemical behaviour as cathode in sodium cells, J. Mater. Chem. 12 (2002) 1142, https://doi.org/10.1039/B108830K.

[21] J. Song, B. Li, Y. Chen, Y. Zuo, F. Ning, H. Shang, G. Feng, N. Liu, C. Shen, X. Ai, D. Xia, A high-performance Li–Mn–O Li-rich cathode material with rhombohedral symmetry via intralayer Li/Mn disordering, Adv. Mater. 32 (2020) 2000190, https://doi.org/10.1002/adma.202000190.

[22] K. Wang, P. Yan, M. Sui, Phase transition induced cracking plaguing layered cathode for sodium-ion battery, Nano Energy 54 (2018) 148, https://doi.org/10.1016/j.nanoen.2018.09.073.

[23] P. Zhou, Z. Che, J. Liu, J. Zhou, X. Wu, J. Weng, J. Zhao, H. Cao, J. Zhou, F. Cheng, High-entropy P2/O3 biphasic cathode materials for wide-temperature rechargeable sodium-ion batteries, Energy Storage Mater. 57 (2023) 618, https://doi.org/10.1016/j.ensm.2023.03.007.

[24] S. Li, L. Yang, Z. Liu, C. Zhang, X. Shen, Y. Gao, Q. Kong, Z. Hu, C.-Y. Kuo, H.-J. Lin, C.-T. Chen, Y. Yang, J. Ma, Z. Hu, X. Wang, R. Yu, Z. Wang, L. Chen, Surface Al-doping for compromise between facilitating oxygen redox and enhancing structural stability of Li-rich layered oxide, Energy Storage Mater. 55 (2023) 356, https://doi.org/10.1016/j.ensm.2022.12.006.

[25] L. Wang, C. Zhang, L. Yang, S. Li, H. Chu, X. Li, Y. Meng, H. Zhuang, Y. Gao, Z. Hu, J.-M. Chen, S.-C. Haw, C.-w. Kao, T.-S. Chan, X. Shen, Z. Wang, R. Yu, Mg substitution induced TM/vacancy disordering and enhanced structural stability in layered oxide cathode materials, ACS Appl. Mater. Interfaces 15 (2023) 11756, https://doi.org/10.1021/acsami.2c21608.

[26] X. Wu, C. Chen, C. Zhao, H. Liu, B. Hu, J. Li, C. Li, B. Hu, Achieving long-enduring high-voltage oxygen redox in P2-structured layered oxide cathodes by eliminating nonlattice oxygen redox, Small 19 (2023). https://www.ncbi.nlm.nih.gov/pubmed/37211714.

[27] Z. Wu, Y. Ni, S. Tan, E. Hu, L. He, J. Liu, M. Hou, P. Jiao, K. Zhang, F. Cheng, J. Chen, Realizing high capacity and zero strain in layered oxide cathodes via lithium dual-site substitution for sodium-ion batteries, J. Am. Chem. Soc. 145 (2023) 9596, https://doi.org/10.1021/jacs.3c00117.

[28] H. Xu, C. Cheng, S. Chu, X. Zhang, J. Wu, L. Zhang, S. Guo, H. Zhou, Anion–cation synergetic contribution to high capacity, structurally stable cathode materials for sodium-ion batteries, Adv. Funct. Mater. 30 (2020) 2005164, https://doi.org/10.1002/adfm.202005164.

[29] E. Pellegrin, L.H. Tjeng, F.M.F. d. Groot, R. Hesper, G.A. Sawatzky, Y. Moritomo, Y. Tokura, Soft X-ray magnetic circular dichroism study of the colossal magnetoresistance compound $La_{1-x}Sr_xMnO_3$, J. Electron. Spectrosc. 86 (1997) 115, https://doi.org/10.1016/S0368-2048(97)00055-8.

[30] A.N. Vasiliev, O.S. Volkova, L.S. Lobanovskii, I.O. Troyanchuk, Z. Hu, L.H. Tjeng, D.I. Khomskii, H.J. Lin, C.T. Chen, N. Tristan, F. Kretzschmar, R. Klingeler, B. Büchner, Valence states and metamagnetic phase transition in partially B-site-disordered perovskite $EuMn_{0.5}Co_{0.5}O_3$, Phys. Rev. B 77 (2008), https://doi.org/10.1103/PhysRevB.77.104442.

[31] N. Hollmann, Z. Hu, T. Willers, L. Bohatý, P. Becker, A. Tanaka, H.H. Hsieh, H. J. Lin, C.T. Chen, L.H. Tjeng, Local symmetry and magnetic anisotropy in multiferroic $MnWO_4$ and antiferromagnetic $CoWO_4$ studied by soft X-ray absorption spectroscopy, Phys. Rev. B 82 (2010), https://doi.org/10.1103/PhysRevB.82.184429.

[32] H. Wu, C.F. Chang, O. Schumann, Z. Hu, J.C. Cezar, T. Burnus, N. Hollmann, N. B. Brookes, A. Tanaka, M. Braden, L.H. Tjeng, D.I. Khomskii, Orbital order in $La0.5Sr1.5MnO4$: beyond a common local Jahn-Teller picture, Phys. Rev. B 84 (2011), https://doi.org/10.48550/arXiv.1104.3717.

[33] Y.-Y. Yin, M. Liu, J.-H. Dai, X. Wang, L. Zhou, H. Cao, C. dela Cruz, C.-T. Chen, Y. Xu, X. Shen, R. Yu, J.A. Alonso, A. Muñoz, Y.-F. Yang, C. Jin, Z. Hu, Y. Long, $LaMn_3Ni_2Mn_2O_{12}$: an A- and B-site ordered quadruple perovskite with A-Site tuning orthogonal spin ordering, Chem. Mater. 28 (2016) 8988, https://doi.org/10.1021/acs.chemmater.6b03785.

[34] H. Liu, J. Zhou, L. Zhang, Z. Hu, C. Kuo, J. Li, Y. Wang, L.H. Tjeng, T.-W. Pi, A. Tanaka, L. Song, J.-Q. Wang, S. Zhang, Insight into the role of metal–oxygen bond and O 2p hole in high-voltage cathode $LiNi_xMn_{2-x}O_4$, J. Phys. Chem. C 121 (2017) 16079, https://doi.org/10.1021/acs.jpcc.7b03875.

[35] S. Nemrava, D.A. Vinnik, Z. Hu, M. Valldor, C.-Y. Kuo, D.A. Zherebtsov, S. A. Gudkova, C.-T. Chen, L.H. Tjeng, R. Niewa, Three oxidation states of manganese in the barium hexaferrite $BaFe_{12-x}Mn_xO_{19}$, Inorg. Chem. 56 (2017) 3861, https://doi.org/10.1021/acs.inorgchem.6b02688.

[36] M. Abbate, F.M.F. de Groot, J.C. Fuggle, A. Fujimori, O. Strebel, F. Lopez, M. Domke, G. Kaindl, G.A. Sawatzky, M. Takano, Y. Takeda, H. Eisaki, S. Uchida, Controlled-valence properties of $La_{1-x}Sr_xFeO_3$ and $La_{1-x}Sr_xMnO_3$ studied by soft X-ray absorption spectroscopy, Phys. Rev. B 46 (1992) 4511, https://doi.org/10.1103/PhysRevB.46.4511.

[37] Y.Y. Chin, Z. Hu, H.J. Lin, S. Agrestini, J. Weinen, C. Martin, S. Hébert, A. Maignan, A. Tanaka, J.C. Cezar, N.B. Brookes, Y.F. Liao, K.D. Tsuei, C.T. Chen, D.I. Khomskii, L.H. Tjeng, Spin-orbit coupling and crystal-field distortions for a low-spin $3d^5$ state in $BaCoO_3$, Phys. Rev. B 100 (2019) 205139. https://link.aps.org/doi/10.1103/PhysRevB.100.205139.

[38] H. Huang, Y.-C. Chang, Y.-C. Huang, L. Li, A.C. Komarek, L.H. Tjeng, Y. Orikasa, C.-W. Pao, T.-S. Chan, J.-M. Chen, S.-C. Haw, J. Zhou, Y. Wang, H.-J. Lin, C.-T. Chen, C.-L. Dong, C.-Y. Kuo, J.-Q. Wang, Z. Hu, L. Zhang, Unusual double ligand holes as catalytic active sites in $LiNiO_2$, Nat. Commun. 14 (2023), https://doi.org/10.1038/s41467-023-37775-4.

[39] Y.H. Zhang, D. Zhang, L.R. Wu, J. Ma, Q. Yi, Z. Wang, X. Wang, Z. Wu, C. Zhang, N. Hu, S.C. Haw, J.M. Chen, Z. Hu, G. Cui, Stabilization of lattice oxygen in Li-rich Mn-based oxides via swing-like non-isothermal sintering, Adv. Energy Mater. 12 (2022), https://doi.org/10.1002/aenm.202202341.

[40] S. Zhang, F. Sun, X. Du, X. Zhang, L. Huang, J. Ma, S. Dong, A. Hilger, I. Manke, L. Li, B. Xie, J. Li, Z. Hu, A.C. Komarek, H.-J. Lin, C.-Y. Kuo, C.-T. Chen, P. Han, G. Xu, Z. Cui, G. Cui, In situ-polymerized lithium salt as a polymer electrolyte for high-safety lithium metal batteries, Energy Environ. Sci. 16 (2023) 2591, https://doi.org/10.1039/D3EE00558E.

[41] J.H. Jung, K.H. Kim, D.J. Eom, T.W. Noh, E.J. Choi, J.J. Yu, Y.S. Kwon, Y. Chung, Determination of electronic band structures of $CaMnO_3$ and $LaMnO_3$ using optical-conductivity analyses, Phys. Rev. B 55 (1997) 15489, https://doi.org/10.1103/PhysRevB.55.15489.

[42] Y. Zuo, H. Shang, J. Hao, J. Song, F. Ning, K. Zhang, L. He, D. Xia, Regulating the potential of anion redox to reduce the voltage hysteresis of Li-rich cathode materials, J. Am. Chem. Soc. 145 (2023) 5174. https://www.ncbi.nlm.nih.gov/pubmed/36757130.

[43] J. Zhou, L. Zhang, Y.-C. Huang, C.-L. Dong, H.-J. Lin, C.-T. Chen, L.H. Tjeng, Z. Hu, Voltage- and time-dependent valence state transition in cobalt oxide catalysts during the oxygen evolution reaction, Nat. Commun. 11 (2020). https://www.nature.com/articles/s41467-020-15925-2.

[44] A. Bianconi, M. Dell'Ariccia, P.J. Durham, J.B. Pendry, Multiple-scattering resonances and structural effects in the X-ray-absorption near-edge spectra of Fe II and Fe III hexacyanide complexes, Phys. Rev. B 26 (1982) 6502, https://doi.org/10.1103/PhysRevB.26.6502.

[45] S. Agrestini, K. Chen, C.Y. Kuo, L. Zhao, H.J. Lin, C.T. Chen, A. Rogalev, P. Ohresser, T.S. Chan, S.C. Weng, G. Auffermann, A. Völzke, A.C. Komarek, K. Yamaura, M.W. Haverkort, Z. Hu, L.H. Tjeng, Nature of the magnetism of iridium in the double perovskite Sr_2CoIrO_6, Phys. Rev. B 100 (2019), https://doi.org/10.1103/PhysRevB.100.014443.

[46] M. Croft, D. Sills, M. Greenblatt, C. Lee, S.-W. Cheong, K.V. Ramanujachary, D. Tran, Systematic Mn d-configuration change in the $La_{12x}Ca_xMnO_3$ system: a Mn K-edge XAS study, Phys. Rev. B 55 (1997) 8726, https://doi.org/10.1103/PhysRevB.55.8726.

[47] K. Zhang, D. Kim, Z. Hu, M. Park, G. Noh, Y. Yang, J. Zhang, V.W. Lau, S.L. Chou, M. Cho, S.Y. Choi, Y.M. Kang, Manganese based layered oxides with modulated electronic and thermodynamic properties for sodium ion batteries, Nat. Commun. 10 (2019) 5203. https://www.ncbi.nlm.nih.gov/pubmed/30617270.

[48] U. Maitra, R.A. House, J.W. Somerville, N. Tapia-Ruiz, J.G. Lozano, N. Guerrini, R. Hao, K. Luo, L. Jin, M.A. Perez-Osorio, F. Massel, D.M. Pickup, S. Ramos, X. Lu, D.E. McNally, A.V. Chadwick, F. Giustino, T. Schmitt, L.C. Duda, M.R. Roberts, P. G. Bruce, Oxygen redox chemistry without excess alkali-metal ions in $Na_{2/3}[Mg_{0.28}Mn_{0.72}]O_2$, Nat. Chem. 10 (2018) 288. https://www.ncbi.nlm.nih.gov/pubmed/29461536.

[49] E. de la Llave, E. Talaie, E. Levi, P.K. Nayak, M. Dixit, P.T. Rao, P. Hartmann, F. Chesneau, D.T. Major, M. Greenstein, D. Aurbach, L.F. Nazar, Improving energy density and structural stability of manganese oxide cathodes for Na-Ion batteries by structural lithium substitution, Chem. Mater. 28 (2016) 9064, https://doi.org/10.1021/acs.chemmater.6b04078.

[50] J. Liu, R. Qi, C. Zuo, C. Lin, W. Zhao, N. Yang, J. Li, J. Lu, X. Chen, J. Qiu, M. Chu, M. Zhang, C. Dong, Y. Xiao, H. Chen, F. Pan, Inherent inhibition of oxygen loss by regulating superstructural motifs in anionic redox cathodes, Nano Energy 88 (2021) 106252. https://www.sciencedirect.com/science/article/pii/S2211285521005073.

[51] J. Zhang, J.B. Kim, J. Zhang, G.H. Lee, M. Chen, V.W. Lau, K. Zhang, S. Lee, C. L. Chen, T.Y. Jeon, Y.W. Kwon, Y.M. Kang, Regulating pseudo-Jahn-Teller effect and superstructure in layered cathode materials for reversible alkali-ion intercalation, J. Am. Chem. Soc. 144 (2022) 7929. https://www.ncbi.nlm.nih.gov/pubmed/35468290.

[52] J. Jin, Y. Liu, X. Zhao, H. Liu, S. Deng, Q. Shen, Y. Hou, H. Qi, X. Xing, L. Jiao, J. Chen, Annealing in argon universally upgrades the Na-storage performance of Mn-based layered oxide cathodes by creating bulk oxygen vacancies, Angew. Chem. Int. Ed. Engl. 62 (2023) e202219230. https://www.ncbi.nlm.nih.gov/pubmed/36780319.